RSC Advances

PAPER

View Article Online
View Journal | View Issue

Cite this: *RSC Adv.*, 2015, **5**, 79624

Recyclable magnetic $CoFe_2O_4$/BiOX (X = Cl, Br and I) microflowers for photocatalytic treatment of water contaminated with methyl orange, rhodamine B, methylene blue, and a mixed dye†

Young In Choi,[a] Young-Il Kim,[a] Dae Won Cho,[a] Jung-Soo Kang,[b] K. T. Leung[b] and Youngku Sohn*[a]

Received 31st August 2015
Accepted 14th September 2015

DOI: 10.1039/c5ra17616f

www.rsc.org/advances

The recycling of photocatalysts and improving their activities by hybridizing two materials are important. Herein, nanosize ferromagnetic (M_s = 62.3 emu g^{-1}) $CoFe_2O_4$ nanoparticles (NPs) were embedded into nanosize-assembled BiOX (X = Cl, Br and I) microflowers and examined by scanning electron microscopy, transmission electron microscopy, X-ray diffraction, UV-visible absorption spectroscopy, Fourier-transform infrared spectroscopy, and photoluminescence spectroscopy. The adsorption and photocatalytic performance of $CoFe_2O_4$/BiOX for methyl orange (MO), rhodamine B (RhB), methylene blue (MB), and a mixed dye (MO + RhB + MB) were examined under UV and visible light irradiation. The adsorption capacity of $CoFe_2O_4$/BiOI for RhB was 160 mg g_{cat}^{-1}, which is significantly larger than the <5 mg g_{cat}^{-1} obtained for $CoFe_2O_4$/BiOCl and $CoFe_2O_4$/BiOBr. The photocatalytic activity was observed in the order of $CoFe_2O_4$/BiOBr < $CoFe_2O_4$/BiOCl < $CoFe_2O_4$/BiOI for RhB. Their adsorption and photocatalytic performances were also investigated with pure MO, pure MB and a mixed dye. MO in the mixed dye was the most easily removed by the catalysts under light exposure. Based on the scavenger tests, h^+ and $^{\bullet}O_2^-$ play major and minor roles in the photodegradation of the dyes, respectively. Although the $^{\bullet}OH$ radical was formed for $CoFe_2O_4$/BiOBr and $CoFe_2O_4$/BiOCl, it has a much smaller role than the other active species.

1. Introduction

The development of efficient photocatalysts and adsorbents has been a major research focus for energy and the environment. As an environmental issue, removing pollutants present in water has been a persistent goal. In recent years, bismuth oxyhalides, BiOX (X = Cl, Br and I), have exhibited good adsorption/photocatalytic performance and been studied extensively.[1–10] A major advantage of these materials is the ease of band gap tuning between 1.7 eV and 3.4 eV by simply changing the (relative amount of) halide ions.[11,12] More recently, hybrid materials with BiOX have been developed to further increase the photocatalytic activity. The enormous hybrid materials include phthalocyanine (CuPc)/BiOCl,[13] Bi_2S_3/BiOCl,[14] Bi/BiOBr$_x$I$_{1-x}$,[15] BiOBr-g-C_3N_4,[16] (Rh, Pd, Pt)/BiOX(Cl, Br, I),[17] Ag–BiOBr,[18] Ag/AgBr/BiOBr,[19] Ag–BiOBr$_x$I$_{1-x}$,[20] $Bi_{24}O_{31}Cl_{10}$,[21] Bi_2WO_6,[22] BiOCl/$Bi_2O_2CO_3$,[23] BiOI/$BiPO_4$,[24] Ag_3PO_4/BiOI,[25] Bi/BiOI,[26] BiOI–MWCNT,[27] Ti–BiOBr,[28,29] and graphene–BiOBr.[30] The development of magnetic photocatalysts are of interest with the benefit of recyclability, even though in some cases, the catalytic activity is degraded after introducing magnetic materials into the host photocatalyst.[31–40] Magnetic $SrFe_{12}O_{19}$ was found to inhibit the growth of BiOCl along the [001] direction to expose the {001} facet. Furthermore, it induced visible light absorption (change in band gap from 3.3 eV to 2.8 eV after loading the magnetic material) and charge separation to increase photocatalytic MB degradation.[32] Yao *et al.* prepared dandelion-like magnetic Fe_3O_4@C@BiOCl and Fe_3O_4@BiOCl composites. They reported that the surface area, adsorption capacity and photocatalytic activity were improved by introducing an interfacial carbon layer between Fe_3O_4 and BiOCl.[33] The total destruction of organic pollutants is important for eliminating pollution by secondary products. Zhang *et al.* solved this problem by synthesizing BiOBr@SiO_2@Fe_3O_4 microspheres through a multi-step synthesis process. They found only one main intermediate during the photocatalytic degradation of 2,2-bis(4-hydroxyphenyl)propane (BPA), where active h^+ and $^{\bullet}OH$ were mainly and partly involved in the direction oxidation, respectively.[34] For a photocatalytic reaction, the role of active species is

[a]*School of Chemistry and Biochemistry, Yeungnam University, Gyeongsan 38541, Republic of Korea. E-mail: youngkusohn@ynu.ac.kr; Fax: +82-53-810-4613; Tel: +82-53-810-2354*

[b]*WATLab and Department of Chemistry, University of Waterloo, Waterloo, Ontario N2L 3G1, Canada*

† Electronic supplementary information (ESI) available. See DOI: 10.1039/c5ra17616f

very important and has been studied extensively using a number of methods, such as LC-MS,[34,41,42] scavenger tests[34] and DMPO (5,5-dimethyl-1-pyrroline *N*-oxide) electron paramagnetic resonance (EPR) spin trapping techniques.[21,31,43]

A literature summary (ESI, Table S1†)[32–40] clearly showed the novelty of the present study. The previously reported BiOX-based magnetic photocatalysts include BiOCl–$SrFe_{12}O_{19}$,[32] Fe_3O_4@C@BiOCl,[33] BiOBr@SiO_2@Fe_3O_4,[34] Fe_3O_4/BiOCl,[35,36] Fe_3O_4@SiO_2@BiOBr,[37] BiOBr/Fe_2O_3,[38] BiOBr–$ZnFe_2O_4$,[39] and Fe_3O_4/BiOI.[40] However, all the catalysts[32,33,35–40] were only tested with pure MO, RhB and MB dyes. There are no reports on a more complicated dye system such as mixed dyes. Because a real polluted area is complicated it is necessary to test a more complicated simulated dye system as presented in this study. The catalysts in the literatures were prepared with only a single BiOX matrix (for example, BiOCl, BiOBr or BiOI) and mainly tested under visible light. However, we prepared magnetic catalysts with three BiOX (for example, BiOCl, BiOBr and BiOI) matrices and tested both under UV and visible light conditions for systematic comparison and analysis.

In the present study, p-type BiOX was first hybridized with n-type $CoFe_2O_4$ to prepare magnetic $CoFe_2O_4$/BiOX (X = Cl, Br and I) composites for the purpose of recycling a photocatalyst and a simulated real water treatment. The catalysts were fully tested with MO, RhB and MB and a mixed dye (MO + RhB + MB) under UV and visible light. Hybridization of two different materials is an important strategy to increase a performance.[32–40,44–48] A deeper understanding of the different roles of the photocatalysts to a more complicated dye system will be very important for developing a photocatalyst applicable to a more complicated system.

2. Experimental section

2.1. Catalysts preparation

For the synthesis of $CoFe_2O_4$ nanoparticles (NPs), stoichiometric amounts (1 : 2 mole ratio) of Co nitrate and Fe nitrate were weighed and dissolved completely in ethylene glycol (EG) solvent. After heating the solution at 160 °C for 1 h, a 0.2 M Na_2CO_3 solution was added and the solution was stirred for 1 h. Subsequently, the solution was cooled naturally and the products were filtered. For the synthesis of $CoFe_2O_4$/BiOX (X = Cl, Br and I) composites, $CoFe_2O_4$ NPs was first dispersed in EG solvent and a stoichiometric amount of $Bi(NO_3)_3 \cdot 5H_2O$ was added. The mole ratio of $CoFe_2O_4$/Bi was fixed to 0.25. A stoichiometric amount of KX (X = Cl, Br and I) was then added. The Bi/X molar ratio was fixed to 1.0. The solution in a tightly capped Teflon bottle was placed at 120 °C in an oven for 5 h. The final products were washed several times with deionized water and ethanol, and fully dried in an oven (80 °C).

2.2. Catalysts characterization

The surface morphology of the hybrid samples was characterized by field-emission scanning electron microscopy (FE-SEM, Hitachi SE-4800). The crystal phase was analyzed by powder X-ray diffraction (XRD, PANalytical X'Pert Pro MPD) using Cu Kα radiation (λ = 0.154056 nm) operated at 40 kV and 30 mA. Transmission electron microscopy (TEM) was used to examine the microstructure of a selected sample placed on a carbon-coated Cu grid. The diffuse UV-Vis absorption spectra were used to measure the band gaps of the powder samples using a SCINCO NeoSys-2000 double beam UV-Vis spectrophotometer. The Fourier-transform infrared (FT-IR, Thermo Scientific Nicolet iS10) spectra were obtained in attenuated total reflection (ATR) mode. The photoluminescence (PL) spectra of the powder samples were obtained using a SCINCO FluoroMate FS-2. Magnetic properties of the powder samples were examined using a MPMS SQUID magnetometer (Quantum Design, USA) with an applied magnetic field ranging from −70 to 70 kOe at room temperature. The Brunauer–Emmett–Teller (BET) surface areas for the powder samples were measured using a ChemBET TPR/TPD analyzer (Quantachrome Instruments, USA) equipped with a thermal conductivity detector.

2.3. Adsorption, photocatalytic activity and active species

For the BiOCl and BiOBr catalysts, a 20 mg L^{-1} RhB solution was used, while for BiOI, a 40 mg L^{-1} dye solution was used. For a mixed dye to test the photocatalytic performance of the BiOCl and BiOBr catalysts, 10 mg L^{-1} concentrations of MO, RhB and MB solutions were mixed. For a mixed dye to test the BiOI catalyst, 20 mg L^{-1} MO, RhB and MB solutions were mixed. For adsorption, 25 mg of a catalyst was dispersed into a 100 mL dye (RhB or the mixed dye) solution. The solution was fully stirred in the dark for 1 hour. The photocatalytic experiments were performed under visible and UV light with different light exposure times. The concentration of the dye solution was monitored using a Jasco V-530 UV-Vis spectrophotometer. A scavenger test was used to examine the roles of active $^{\bullet}OH$ and $^{\bullet}O_2^-$ species. Isopropyl alcohol (IPA) and benzoquinone (BQ) were added to the test solution as $^{\bullet}OH$ and $^{\bullet}O_2^-$ scavengers, respectively.[49,50] To examine $^{\bullet}OH$ radical formation over the catalysts, photoluminescence spectroscopy was performed using a terephthalic acid solution.[34] A catalyst was dispersed in the terephthalic acid solution and irradiated with UV or visible light for a specified time. The PL spectrum of the solution was taken at an excitation wavelength of 315 nm using a SCINCO FluoroMate FS-2 fluorometer.

3. Results and discussion

3.1. Morphologies

Fig. 1 presents SEM images of the $CoFe_2O_4$/BiOX nano-assembled microflowers prepared in EG. The SEM images commonly showed distorted spheres with sizes of 1–3 μm. The assembled average sizes were in the order of $CoFe_2O_4$/BiOCl < $CoFe_2O_4$/BiOI < $CoFe_2O_4$/BiOBr. The magnified SEM images showed that the spheres differed slightly according to halide ions used and consisted of nanosize structures. The reported surface areas of bare BiOCl, BiOBr and BiOI microflowers were 17 m^2 g^{-1}, 19 m^2 g^{-1} and 61 m^2 g^{-1}, respectively (Table 1).[11,12] The similar surface areas for BiOCl and BiOBr may indicate that they had similar morphological structures as shown in Fig. 1.

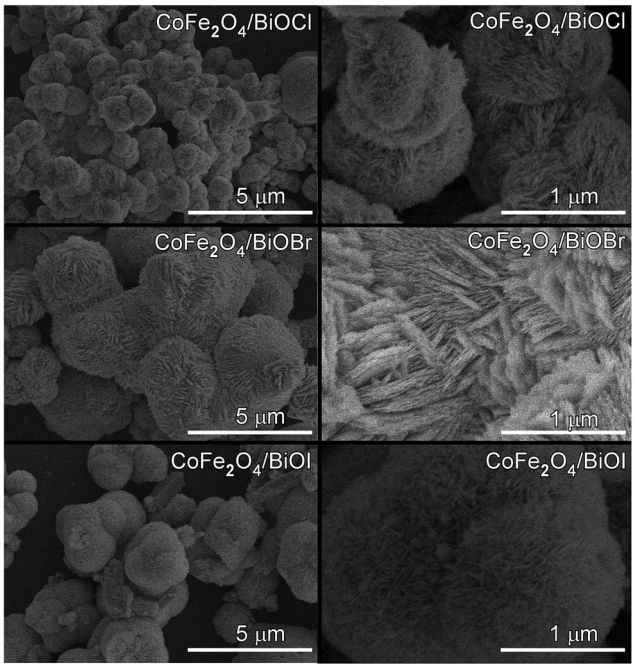

Fig. 1 SEM images of $CoFe_2O_4$/BiOX (X = Cl, Br and I) nano-assembled microflowers.

Table 1 BET surface areas ($m^2\ g^{-1}$) of BiOX before and after loading $CoFe_2O_4$ NPs

Catalysts	BiOCl	BiOBr	BiOI	Ref.
Before loading	17	19	61	11 and 12
After loading NPs	32.7	30.9	62.0	This work

Upon loading $CoFe_2O_4$ NPs, we observed the BET surface areas of 32.7 $m^2\ g^{-1}$, 30.9 $m^2\ g^{-1}$ and 62.0 $m^2\ g^{-1}$ for $CoFe_2O_4$/BiOCl, $CoFe_2O_4$/BiOBr and $CoFe_2O_4$/BiOI, respectively (Table 1). The surface areas of BiOCl and BiOBr were substantially increased while that of BiOI showed no significant change after loading $CoFe_2O_4$ NPs. The BiOCl and BiOBr with smaller surface areas could be increased a lot further by loading with smaller size $CoFe_2O_4$ NPs.

Fig. 2 shows TEM images of the selected $CoFe_2O_4$/BiOI microflowers and $CoFe_2O_4$ nanoparticles (NPs). The energy-dispersive X-ray (EDX) analysis confirmed the chemical species of the $CoFe_2O_4$ NPs and the hybrid materials (ESI, Fig. S1†). The magnetic $CoFe_2O_4$ NPs were very small with sizes of <5 nm. The 3D-microflowers were formed by the assembly of nanosize structures. The BiOX seeds were formed *via* the reaction, $Bi^{3+} + X^- + H_2O \rightarrow BiOX + 2H^+$. The nano-seeds assemble and grow into a larger sphere through Ostwald ripening.[8] During this growth, the initially dispersed much smaller NPs (unreactive to BiOX) became embedded into the μm-size BiOI microflowers to form hybrid $CoFe_2O_4$/BiOI microflowers. Upon completion of the growth, BiOX microflowers generally showed {011} and {020} crystalline lattices, indicating higher percentage of {001} facets.[11,12] In the HRTEM image of Fig. 2, a clear lattice

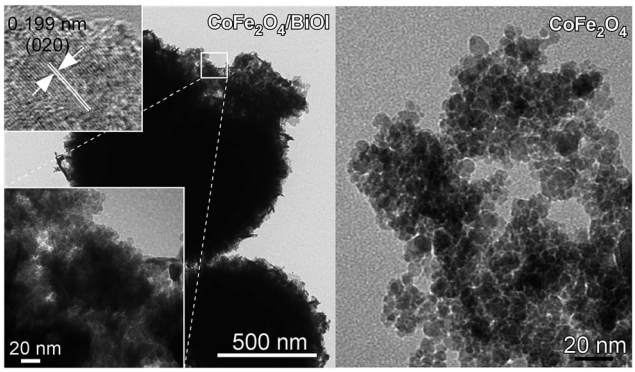

Fig. 2 Typical TEM images of the $CoFe_2O_4$/BiOI microflowers and $CoFe_2O_4$ nanoparticles. Left top inset shows the HRTEM image of the edge of BiOI.

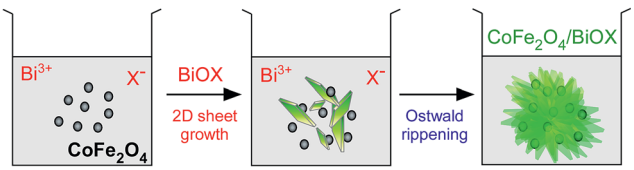

Scheme 1 Growth mechanism of the hybrid materials.

fringe with a spacing of 0.199 nm corresponds to the (020) plane of tetragonal BiOI (Scheme 1).[12]

3.2. Crystal structures

Fig. 3 shows the powder XRD patterns of $CoFe_2O_4$ NPs and $CoFe_2O_4$/BiOX (X= Cl, Br and I) microflowers. The XRD patterns of pure $CoFe_2O_4$ NPs were relatively weaker than those of the microflowers due to the lower crystallinity arising from the extremely small NP size (<5 nm). The patterns matched those of cubic ($Fd\bar{3}m$) $CoFe_2O_4$ (JCPDS 3-0864). The peaks at $2\theta = 34.8°$ and 60.5° were assigned to the (311) and (440) planes of the

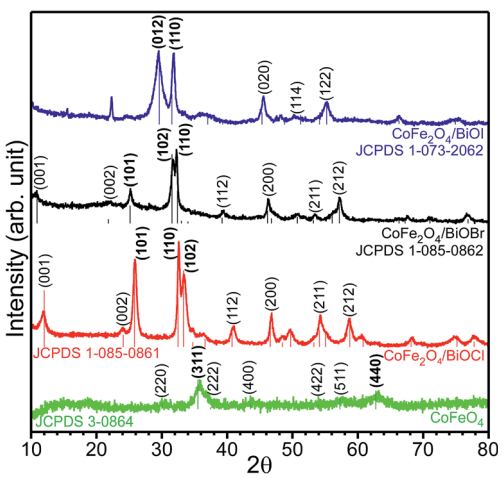

Fig. 3 Power X-ray diffraction patterns of $CoFe_2O_4$ NPs, and $CoFe_2O_4$/BiOX (X = Cl, Br and I) microflowers.

crystal structure. The other peaks included the (220), (222), (400), (422), and (511) planes. For the $CoFe_2O_4$/BiOX (X = Cl, Br and I) microflowers, the XRD peaks of $CoFe_2O_4$ NPs could not be discriminated clearly because of the smaller hybrid amount in the BiOX matrices and the weak XRD peaks of pure $CoFe_2O_4$ NPs. The XRD patterns of $CoFe_2O_4$/BiOCl were similar to those of tetragonal (*P*4/*nmm*) BiOCl (JCPDS 1-085-0861). Three major peaks were observed at $2\theta = 25.9°$, 32.6° and 36.4°, which were assigned to the (101), (110) and (102) planes of the tetragonal phase, respectively. The XRD patterns of $CoFe_2O_4$/BiOBr matched those of tetragonal (*P*4/*nmm*) BiOBr (JCPDS 01-085-0862). Two major peaks at $2\theta = 31.7°$ and 32.3° were assigned to the (102) and (110) planes, respectively. The XRD peak of the (101) plane was relatively weaker. For the $CoFe_2O_4$/BiOI microflowers, the XRD peaks matched those of tetragonal (*P*4/*nmm*) BiOI (JCPDS 1-073-2062). Two major peaks were observed at $2\theta = 29.5°$ and 31.8° corresponding to the (012) and (110) planes, respectively.

3.3. Optical properties

Fig. 4 shows the UV-Vis diffuse reflectance (DR) absorption spectra of $CoFe_2O_4$/BiOX (X = Cl, Br and I) microflowers. The *Y*-axis (absorbance) was obtained from the DR data using the Kubelka–Munk method. The sharp absorption edges (not shown) for bare BiOCl, BiOBr and BiOI microflowers were observed at 3.2, 2.8 and 1.8 eV, respectively. Upon loading the $CoFe_2O_4$ NPs, the absorption in the visible region were increased substantially and the colors of the samples became darker. We could expect a change in color and an increase in visible light absorption upon introducing black color $CoFe_2O_4$ NPs with a band gap of 1.2 eV. An increase in visible light absorption facilitates photocatalytic activity under visible light.[51] Although the visible light absorption of bare BiOCl and BiOBr microflowers was much lower than that of BiOI, the absorption became higher than BiOI after loading the $CoFe_2O_4$ NPs. Upon embedding $CoFe_2O_4$ NPs, the $CoFe_2O_4$/BiOX microflowers showed magnetic properties (as shown in the inset photos in Fig. 4).

Fig. 5 shows the photoluminescence (PL) spectra of $CoFe_2O_4$/BiOX (X = Cl, Br and I) microflowers taken at an excitation wavelength of 250 nm. The origin of the PL is the recombination of an electron and a hole. A higher the PL intensity indicates more recombination. Higher recombination indicates poor charge separation, generally leading to lower catalytic activity.[52] The PL spectra of the three different samples were quite different with an intensity in the order of $CoFe_2O_4$/BiOI < $CoFe_2O_4$/BiOBr < $CoFe_2O_4$/BiOCl. As the band gap is larger (or the excitation energy is closer to the CB of a material), the PL becomes stronger. In other words, the band gap edge shifts to a longer wavelength as the halide ion is changed from Cl, Br to I. As a consequence, the PL peak maximum is shifted to a longer wavelength. For the $CoFe_2O_4$/BiOCl microflowers, broad regions were observed between 320 nm and 600 nm. For $CoFe_2O_4$/BiOBr, a broad peak at 460 nm was dominant. This was attributed to defects. For $CoFe_2O_4$/BiOI, the intensity decreased dramatically. A broad maximum was observed at 600 nm.

FT-IR spectra (ESI, Fig. S2†) were taken for $CoFe_2O_4$/BiOX (X = Cl, Br and I) and BiOX microflowers. Several peaks were observed and the profiles were similar before and after loading the $CoFe_2O_4$ NPs. A broad peak at 3400 cm^{-1} and a sharper peak at 1600 cm^{-1} were attributed to the stretching and deformation vibrations of the adsorbed OH group.[32]

3.4. Magnetic properties

The magnetic properties of $CoFe_2O_4$ NPs and $CoFe_2O_4$/BiOX (X = Cl, Br and I) microflowers were examined by SQUID. Fig. 6 shows the magnetization (*M*–*H*) curves measured with magnetic fields from −70 to 70 kOe at room temperature. The *M*–*H* curves commonly showed saturation magnetization (M_s). A saturation magnetization of 0.0623 emu mg^{-1} (or 62.3 emu g^{-1}) was measured for $CoFe_2O_4$ NPs. This value was in good agreement with the literature.[44] A magnetic hysteresis loop was observed (ESI, Fig. S3†), suggesting ferromagnetic behavior of the NPs. The hysteresis loop became significantly narrower for the hybrid materials. For $CoFe_2O_4$/BiOCl, $CoFe_2O_4$/BiOBr and $CoFe_2O_4$/BiOI microflowers, the magnetization values were

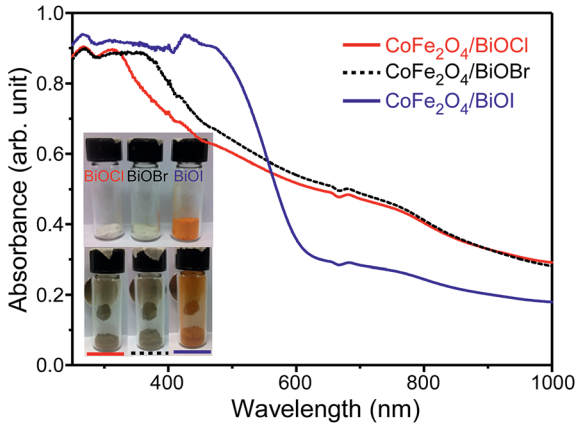

Fig. 4 UV-visible diffuse reflectance absorption spectra of $CoFe_2O_4$/BiOX (X = Cl, Br and I) microflowers. The insets show photographs of the corresponding samples.

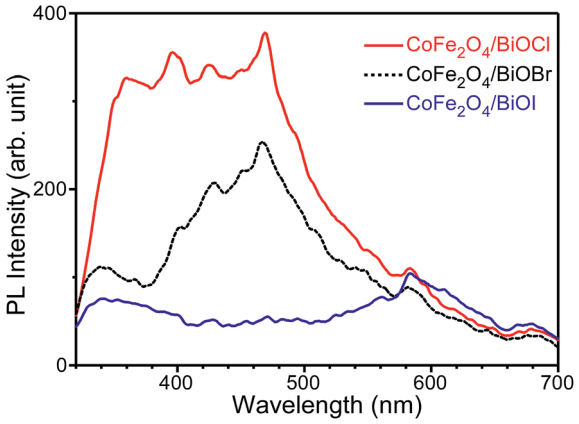

Fig. 5 Photoluminescence spectra of $CoFe_2O_4$/BiOX (X = Cl, Br and I) microflowers at an excitation wavelength of 250 nm.

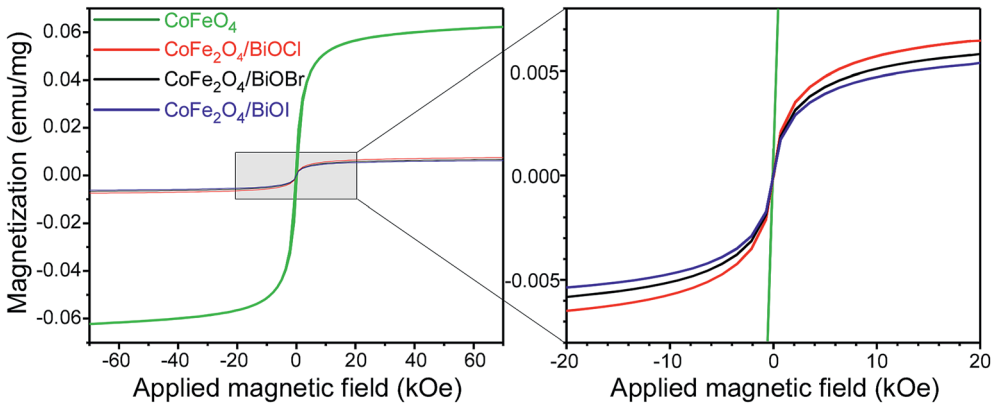

Fig. 6 Magnetization (M–H) curves for $CoFe_2O_4$ NPs and $CoFe_2O_4$/BiOX (X = Cl, Br and I) microflowers with applied magnetic fields from −70 to 70 kOe at room temperature.

decreased and measured to be 0.00747, 0.0067 and 0.00621 emu mg^{-1} (or 7.47, 6.7 and 6.21 emu g^{-1}), respectively. The decrease in saturation magnetization is due to hybridization with non-magnetic BiOX (X = Cl, Br and I) materials.[44,47] Although the magnetization of the hybrid sample was decreased[44,47] the powder sample dispersed in a dye solution was easily (in a few seconds) attracted (or recycled) by a magnet (ESI, Fig. S4†).

3.5. Adsorption and photocatalytic activity of $CoFe_2O_4$/BiOCl and $CoFe_2O_4$/BiOBr for pure RhB

The adsorption and photocatalytic activities of $CoFe_2O_4$/BiOCl microflowers for RhB were tested. Fig. 7 shows the UV-Vis absorption spectra of RhB tested with the catalysts under visible (Fig. 7A–C) and UV (Fig. 7A1, B1 and C1) light irradiation. The roles of active $^{\bullet}O_2^-$ and $^{\bullet}OH$ radical species were also examined using a scavenger test method. Benzoquinone (BQ) and isopropyl alcohol (IPA) were added as $^{\bullet}O_2^-$ and $^{\bullet}OH$ scavengers, respectively. RhB showed a broad UV-Vis absorption band at approximately 550 nm. The peak decreased after adsorption over the catalyst for 1 hour under dark conditions. Under visible light without a scavenger (Fig. 7A), with increasing light exposure time, the UV-Vis absorption peak decreased substantially and the peak position shifted gradually to a shorter wavelength of 490 nm. The pink color of the original solution changed to a green color. This indicates that a secondary product had formed during the photocatalytic reaction of RhB over the catalyst. After visible light irradiation for 6 h, >95% of the RhB was degraded. The blue-shift in the peak for RhB is generally attributed to de-ethylation products by $^{\bullet}O_2^-$

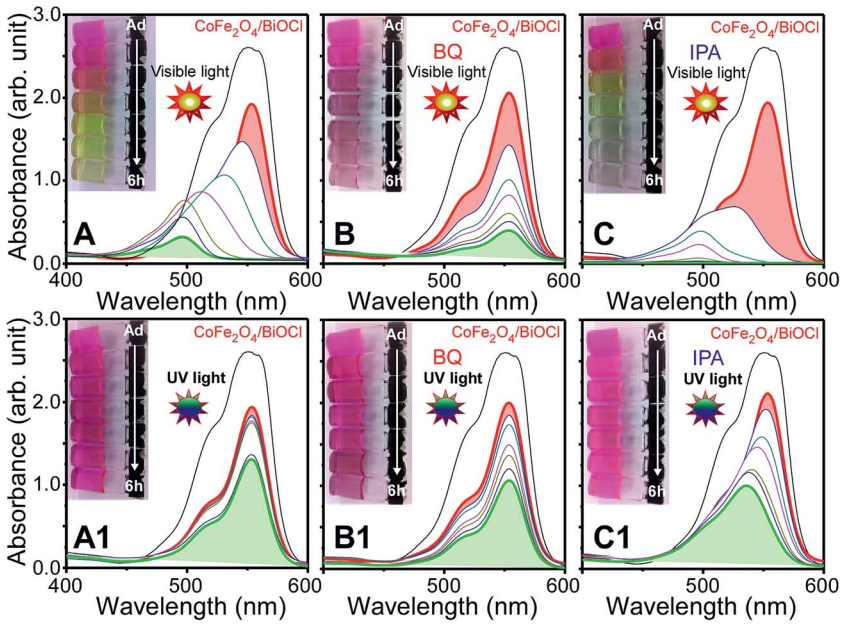

Fig. 7 Adsorption (in dark) and photodegradation (under UV and visible lights) tests of RhB (20 mg L^{-1}, 100 mL) over 25 mg $CoFe_2O_4$/BiOCl microflowers without (A and A1) and with scavengers of BQ (B and B1) and IPA (C and C1). The insets show the corresponding photographs displaying a change in the dye color with photodegradation time.

radical species.[12,20,38] To confirm this, benzoquinone (BQ) was added as a $^{\bullet}O_2^-$ radical scavenger and the photocatalytic experiments were performed (Fig. 7B). Although the peak intensity decreased with increasing light exposure time, the peak position showed no change. Based on the results, it was concluded that the $^{\bullet}O_2^-$ radical was involved in the photocatalytic reaction, but it did not affect the dye degradation greatly. To test the role of $^{\bullet}OH$ radical species, IPA was added to the catalyst solution during photoirradiation (Fig. 7C). The UV-Vis absorption peak decreased with increasing irradiation time, and changed its peak position. After adding IPA, the degradation rate was increased slightly due to the greater dispersion of the catalysts. The scavenger did not negate the photodegradation rate. This suggests that the $^{\bullet}OH$ radical was not involved in the photocatalytic reaction. Li *et al.* also obtained a similar result for RhB over Fe_3O_4/BiOI and reported that h^+ and $^{\bullet}O_2^-$ were the major active species while $^{\bullet}OH$ was a minor species for dye degradation.[40] Under UV irradiation, the degradation rate decreased and no shift in the peak position was observed (Fig. 7A1). This suggests that the $^{\bullet}O_2^-$ radical was not involved significantly in the photocatalytic reaction (Fig. 7B1). After adding the $^{\bullet}OH$ radical scavenger (Fig. 7C1), IPA, a shift in the peak position under UV light irradiation with time was observed.

The adsorption and photocatalytic activity of the $CoFe_2O_4$/BiOBr microflowers for RhB were examined by UV-Vis absorption spectroscopy (ESI, Fig. S5†). As discussed above, the catalysts were tested with and without active species scavengers under UV and visible light irradiation. The behaviors of the UV-Vis absorption spectra were similar to those of the $CoFe_2O_4$/BiOCl microflowers. The adsorption performance of the $CoFe_2O_4$/BiOBr microflowers was somewhat lower than that of $CoFe_2O_4$/BiOCl microflowers. In addition, the photocatalytic activity was also lower than that of the $CoFe_2O_4$/BiOCl microflowers. After adding BQ and IPA, similar results to those for the $CoFe_2O_4$/BiOCl microflowers were obtained.

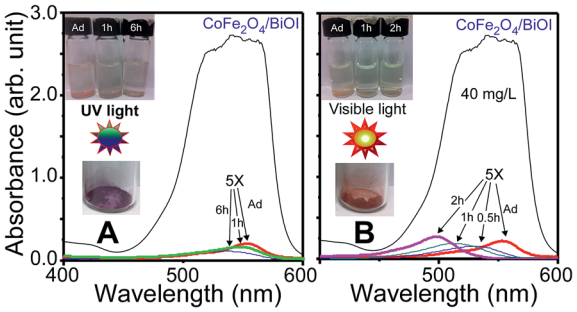

Fig. 8 Adsorption (in dark) and photocatalytic dye degradation ((A) under UV light, (B) under visible light) of Rh B (40 mg L^{-1}, 100 mL) over 25 mg $CoFe_2O_4$/BiOI microflowers. The insets show photographs of the corresponding solutions showing a change in dye color with photoirradiation time. The weak peaks were multiplied by 5×.

3.6. Adsorption and photocatalytic activity of $CoFe_2O_4$/BiOI for pure RhB

Fig. 8 displays the UV-Vis absorption spectra of RhB solution (40 mg L^{-1}) over $CoFe_2O_4$/BiOI microflowers upon adsorption and with UV (Fig. 8A) and visible (Fig. 8B) according to the light exposure time. The adsorption capacity of the catalyst for RhB was extremely high (160 mg g_{cat}^{-1}). The high adsorption performance was attributed to a high surface area and electrostatic interactions between the catalyst and RhB.[11,12,53] The negatively charged $CoFe_2O_4$/BiOI surface may interact strongly with the positively charged RhB.[11,12] Because of the high adsorption capacity, visible light is absorbed mainly by the uppermost adsorbed RhB. The UV absorption by the catalyst is also protected by the adsorbed RhB. Because of the UV

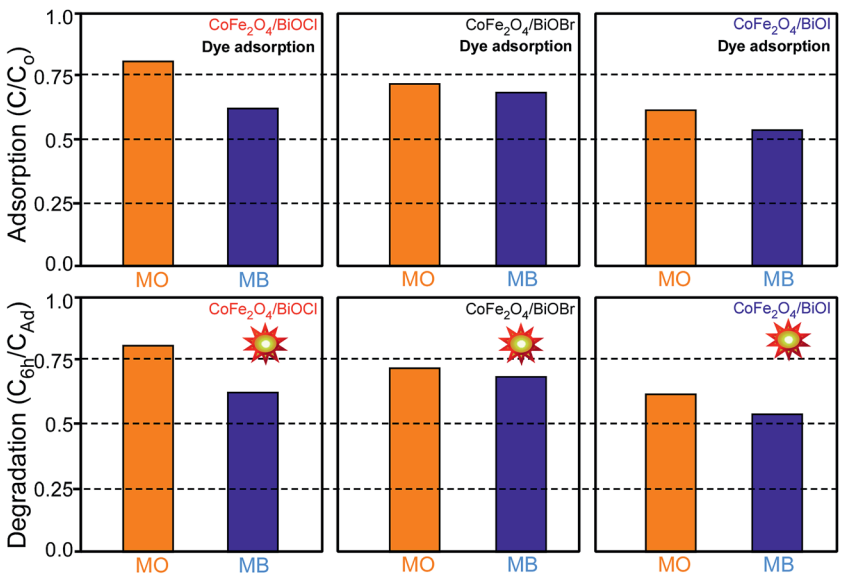

Fig. 9 Adsorption (C/C_o) and photocatalytic dye degradation (C_{6h}/C_{Ad}) performances for pure MO and MB over the $CoFe_2O_4$/BiOX (X = Cl, Br, I) microflowers. C_{Ad} and C_{6h} are the UV-Visible absorption intensities after adsorption and 6 h visible light photoirradiation.

protection, the adsorbed dye was photodegraded slowly (Fig. 8A). As the visible light exposure time was increased, the extremely weak peak was shifted to a shorter wavelength (Fig. 8B). This suggests that the RhB was de-ethylated by active $^{\bullet}O_2^-$ species. Under UV light (Fig. 8A), the shift in the peak position was much slower, indicating dull photodegradation. The catalyst sample after the UV light experiments was much darker than that after the visible light experiments.

3.7. Adsorption and photocatalytic activity of $CoFe_2O_4$/BiOX for pure MO and MB

We tested the adsorption and photocatalytic performances with pure MO and MB for comparison (ESI, Fig. S6†). Fig. 9 displays adsorption (C/C_o) photocatalytic dye degradation (C_{6h}/C_{Ad}) performances for pure MO and MB over the $CoFe_2O_4$/BiOX (X = Cl, Br, I) microflowers under visible light irradiation. For pure MO, the adsorption and photocatalytic degradation performances showed an order of $CoFe_2O_4$/BiOCl < $CoFe_2O_4$/BiOBr < $CoFe_2O_4$/BiOI. For pure MB, the adsorption and photocatalytic degradation performances became an order of $CoFe_2O_4$/BiOBr < $CoFe_2O_4$/BiOCl < $CoFe_2O_4$/BiOI. Because the surface area of $CoFe_2O_4$/BiOI was larger than those of $CoFe_2O_4$/BiOCl and $CoFe_2O_4$/BiOBr (Table 1) it was expected that the adsorption and photocatalytic degradation performances were higher for the $CoFe_2O_4$/BiOI microflowers. For MO, the adsorption and photocatalytic degradation performances of $CoFe_2O_4$/BiOCl was poor than those of $CoFe_2O_4$/BiOBr although the surface area of $CoFe_2O_4$/BiOCl was somewhat larger than that of $CoFe_2O_4$/BiOBr. This reflects that other factors such as surface interactions play also important role in the adsorption and photocatalytic dye degradation.[11,12,53] The adsorption capacities of $CoFe_2O_4$/BiOI for MO and MB were measured to be 24 and 21 mg g_{cat}^{-1}, respectively. This value was significantly smaller than that (160 mg g_{cat}^{-1}) for RhB, as mentioned above.

3.8. Adsorption and photocatalytic activity of $CoFe_2O_4$/BiOX for a mixed dye

The adsorption and photocatalytic performances of the $CoFe_2O_4$/BiOCl (Fig. 10A and A1), $CoFe_2O_4$/BiOBr (Fig. 10B and B1), $CoFe_2O_4$/BiOI (Fig. 10C and C1) microflowers for a mixed dye (MO + RhB + MB) were tested under UV (Fig. 10A–C) and visible (Fig. 10A1, B1 and C1) light and the results are displayed in Fig. 10. The mixed dye showed the absorptions of MO, RhB and MB as expected. The three peak positions of 450, 550 and 650 nm correspond to the MO, RhB and MB dyes, respectively. For the analysis, the three peak positions were selected and the heights of the peaks were examined. Upon adsorption of the mixed under the dark conditions, the UV-Vis absorption peak decreased. The adsorption performance of the mixed dye showed an order of $CoFe_2O_4$/BiOBr < $CoFe_2O_4$/BiOCl ≪ $CoFe_2O_4$/BiOI. On the other hand, the three peaks over the catalyst were not evenly decreased. Fig. 11 shows the adsorption performance of the $CoFe_2O_4$/BiOX (X = Cl, Br and I) microflowers. In the mixed dye, MO showed the best adsorption over the $CoFe_2O_4$/BiOCl (Fig. 11A) and $CoFe_2O_4$/BiOBr (Fig. 11B) microflowers, whereas MB showed the best adsorption over the

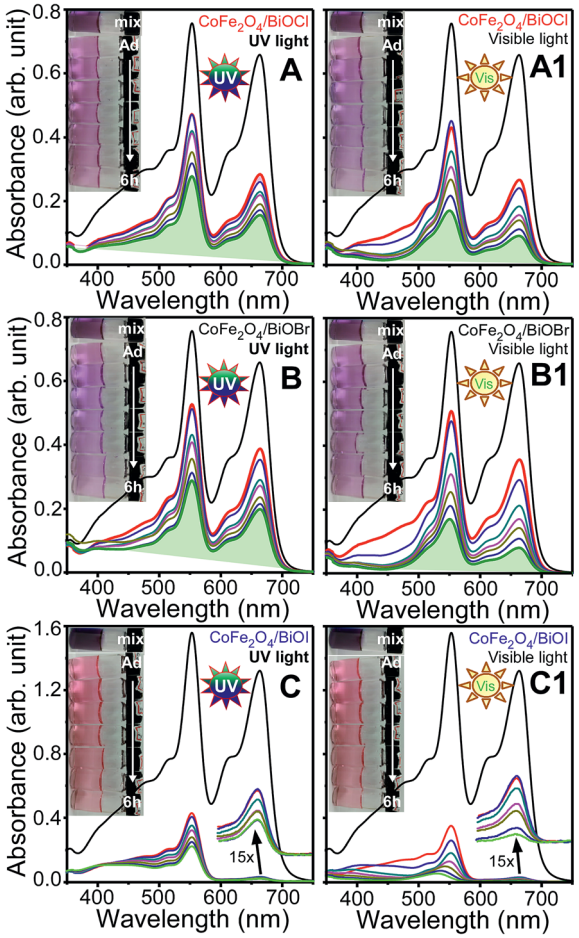

Fig. 10 Adsorption (in dark) and photodegradation (under UV and visible lights) tests of the mixed dye (MO + RhB + MB) over 25 mg $CoFe_2O_4$/BiOX (X = Cl, Br and I) microflowers. For $CoFe_2O_4$/BiOCl (A and A1) and $CoFe_2O_4$/BiOBr (B and B1), a dye mixed with the three dyes with a concentration of 10 mg L^{-1} (=ppm) was used. For $CoFe_2O_4$/BiOI (C and C1), a dye mixed with the three dyes with a concentration of 20 mg L^{-1} was used. The insets show photographs of the corresponding dye solutions as a function of the photodegradation time. The weak peaks were multiplied by 15.

$CoFe_2O_4$/BiOI microflowers (Fig. 11C). MB was almost completely removed by the $CoFe_2O_4$/BiOI microflowers. In contrast, RhB was the most poorly adsorbed on the $CoFe_2O_4$/BiOX microflowers. Because of the relative difference in the adsorption performances over the catalysts, the mixed solutions

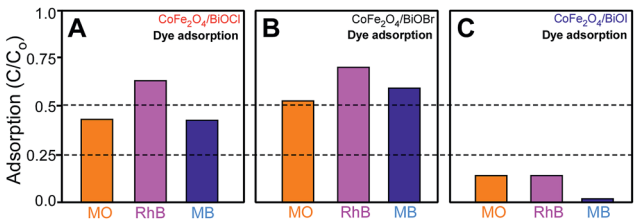

Fig. 11 Adsorption performance of the mixed dye (MO + RhB + MB) over the $CoFe_2O_4$/BiOCl (A), $CoFe_2O_4$/BiOBr (B) and $CoFe_2O_4$/BiOI (C) microflowers.

tested with $CoFe_2O_4$/BiOBr and $CoFe_2O_4$/BiOCl became violet while that with $CoFe_2O_4$/BiOI was pink after the adsorption in the dark condition.

Fig. 12 displays the photodegradation rates of a mixed dye over $CoFe_2O_4$/BiOX (Cl, Br, I) microflowers based on Fig. 10. As the UV (Fig. 12A–C) and visible (Fig. 12A1, B1 and C1) light exposure times were increased, the UV-Vis absorption peaks were decreased. The catalytic activity for MO degradation under UV light (Fig. 12A) was observed in the order of $CoFe_2O_4$/BiOI < $CoFe_2O_4$/BiOCl < $CoFe_2O_4$/BiOBr. For RhB (Fig. 12B) and MB (Fig. 12C), the catalytic activities were similar. For MO in the mixed dye under visible light (Fig. 12A1), the catalytic activity showed a same order of $CoFe_2O_4$/BiOI < $CoFe_2O_4$/BiOCl < $CoFe_2O_4$/BiOBr. However, for RhB (Fig. 12B1) and MB (Fig. 12C1) under visible light irradiation, the order became $CoFe_2O_4$/BiOCl ≤ $CoFe_2O_4$/BiOBr < $CoFe_2O_4$/BiOI. Based on the degradation rates of MO, RhB and MB over the photocatalysts in the mixed dye, MO was degraded most rapidly under visible light irradiation. The order of catalytic activity can be explained as follows. The catalytic activity showed no linear relationship with the BET surface area (Table 1). This indicates that other factors (*e.g.* exposed crystal facets, surface interactions, charge transfer, and energy level alignment) play more important role in the dye degradation than the surface area. It was reported that exposed crystal facets showed different catalytic reactivity for UV and visible light because the wavelength of incident light determines charge transfer direction. A charge transfer rate is very important for photocatalytic dye degradation.[11,12] Different molecules are differently interacted with the different crystal facets and the energy levels (lowest unoccupied/highest occupied molecular orbitals and conduction/valence bands) are differently realigned. The charge transfer rate is promoted by a well-aligned energy level (or a good interfacial wavefunction mixing).

3.9. ˙OH radical formation probed by PL

The formation of ˙OH radicals over the catalysts during photoirradiation was probed by photoluminescence (PL) spectroscopy.[34] A catalyst is dispersed in a terephthalic acid (TA) solution and irradiated with UV (or visible) light while stirring. When a ˙OH radical is formed, TA reacts with the radical to form 2-hydroxyterephthalic acid, which emits a blue emission signal at approximately 425 nm. The intensity of the emission peak reflects the amounts of ˙OH radical produced during photoirradiation. Fig. 13 shows the photoluminescence spectra taken after UV and visible light irradiation for 6 h. For $CoFe_2O_4$/BiOCl and $CoFe_2O_4$/BiOBr, the photoluminescence signal was increased significantly under UV irradiation, while the intensity under visible light was observed to be weaker. Zhang *et al.* also reported ˙OH radical formation under visible light for

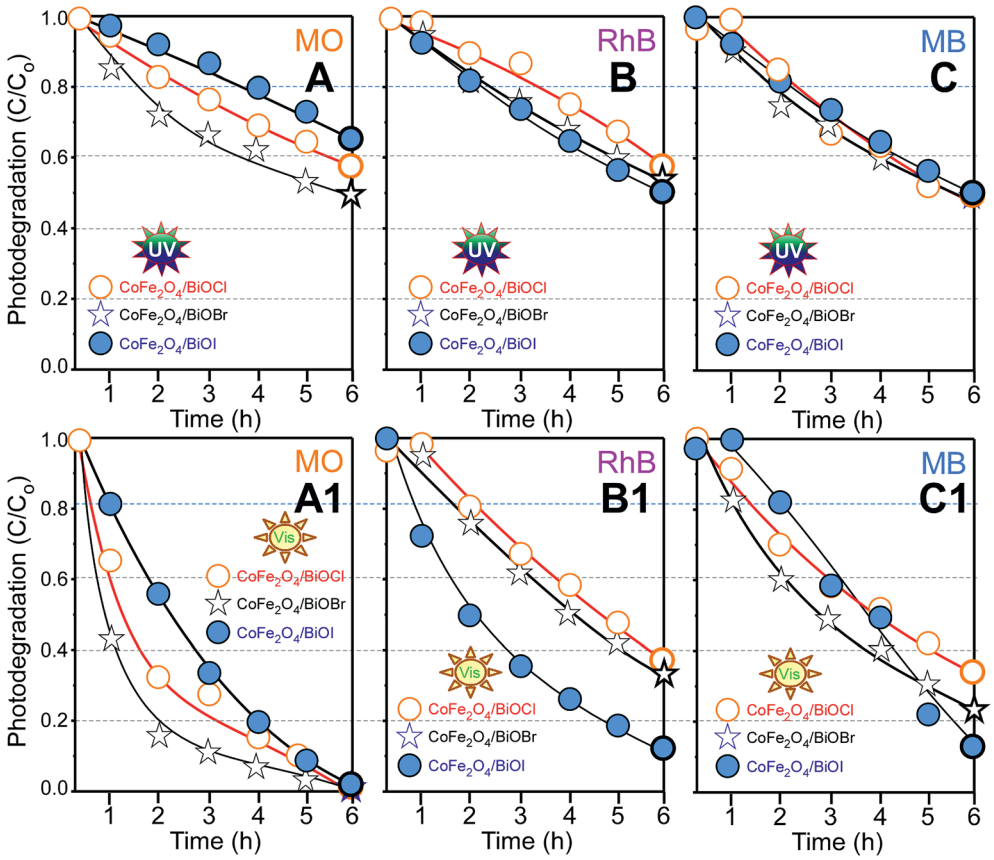

Fig. 12 Photodegradation rates of MO (A and A1), RhB (B and B1) and MB (C and C1) dyes in the mixed dye over $CoFe_2O_4$/BiOX (Cl, Br, I) microflowers under UV (top: A, B and C) and visible (bottom: A1, B1 and C1) light.

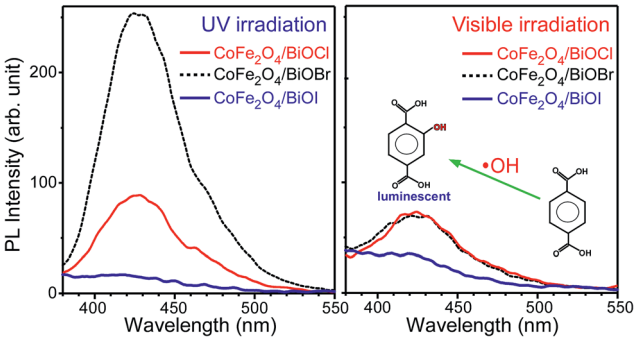

Fig. 13 Photoluminescence spectra of a terephthalic acid solution over the $CoFe_2O_4$/BiOX (X = Cl, Br and I) microflowers after UV (left) and visible (right) light irradiation for 6 h.

BiOBr@SiO_2@Fe_3O_4 microflowers.[34] For $CoFe_2O_4$/BiOI, no photoluminescence signal was observed under UV and visible light irradiation, indicating no $^{\bullet}OH$ radical formation. Under UV light, the PL intensity for $CoFe_2O_4$/BiOBr was stronger than that for $CoFe_2O_4$/BiOCl. Under visible light irradiation, the intensities became similar.

3.10. Photocatalytic mechanism and reliability/stability

The following photocatalytic degradation mechanism (as shown in Fig. 14) can be proposed based on the present results and the literature.[41,49–51,54–63] Three active species of hydroxyl radicals ($^{\bullet}OH$), superoxide radicals ($^{\bullet}O_2^-$) and holes (h^+) act as the major species for photocatalytic dye degradation.

Under UV or visible light irradiation:

$$\text{Mixed and RhB dyes} + \text{visible light} \rightarrow \text{Dye } (e_{CB}^- + h_{VB}^+)$$

$$\text{BiOBr (partly) and BiOI} + \text{visible light} \rightarrow \text{BiOI and BiOBr } (e_{CB}^- + h_{VB}^+)$$

$$CoFe_2O_4 + \text{UV and visible lights} \rightarrow CoFe_2O_4\ (e_{CB}^- + h_{VB}^+)$$

$$CoFe_2O_4/\text{BiOX} + \text{UV light} \rightarrow CoFe_2O_4/\text{BiOX}\ (e_{CB}^- + h_{VB}^+)$$

$$\text{Dye } (e_{CB}^- + h_{VB}^+) + CoFe_2O_4/\text{BiOX} \rightarrow CoFe_2O_4/\text{BiOX}\ (e_{CB}^-) + \text{dye } (h_{VB}^+)$$

$$CoFe_2O_4\ (e_{CB}^- + h_{VB}^+) + \text{BiOX} \rightarrow \text{BiOX}\ (e_{CB}^-) + CoFe_2O_4\ (h_{VB}^+)$$

$$CoFe_2O_4/\text{BiOX}\ (e_{CB}^-) + O_2 \rightarrow {}^{\bullet}O_2^- + CoFe_2O_4/\text{BiOX}$$

$$CoFe_2O_4/\text{BiOX}\ (e_{CB}^-) + {}^{\bullet}O_2^- + 2H^+ \rightarrow 2{}^{\bullet}OH$$

$$CoFe_2O_4/\text{BiOX}\ (h_{VB}^+) + H_2O \rightarrow H^+ + {}^{\bullet}OH + CoFe_2O_4/\text{BiOX}$$

$$\text{Dye} + {}^{\bullet}O_2^-, h^+ \text{ or } {}^{\bullet}OH + \text{dye} \rightarrow \text{degradation}$$

Under visible light irradiation, the dye and the catalyst (with a lower band gap) absorb light to create an electron and a hole in the conduction and valence bands (CB and VB) of the materials, respectively. BiOI (E_g = 1.8 eV) and BiOBr (E_g = 2.8 eV) strongly and partly absorb visible light, respectively. BiOCl (3.2 eV) does not absorb visible light. The electron in the CB of the dye transfers to that of the BiOX material. This is often called a dye-sensitized mechanism. $CoFe_2O_4$ (E_g = 1.2 eV) also absorbs visible light well,[64] and electron in the CB of the $CoFe_2O_4$ transfers to that of BiOX. The electron in the CB is captured by adsorbed oxygen (an electron acceptor) to produce active $^{\bullet}O_2^-$ species. Active $^{\bullet}OH$ radicals can be produced by the reactions of $^{\bullet}O_2^-$ species and electron (e_{CB}^-) or water and hole (h_{VB}^+). The active $^{\bullet}O_2^-$, h^+ and $^{\bullet}OH$ species will consequently degrade the adsorbed dye. The $CoFe_2O_4$/BiOI microflowers showed no creation of $^{\bullet}OH$ radical species while $CoFe_2O_4$/BiOCl and $CoFe_2O_4$/BiOBr formed some $^{\bullet}OH$ radical species. Under visible light, the amount formed was very small compared to that under visible light. Based on the results discussed above, the role of the $^{\bullet}OH$ radical was much weaker than that of the other active species. The role of $^{\bullet}O_2^-$ species depends on the amount of oxygen dissolved in the dye solution.[65] In the present study, $^{\bullet}O_2^-$ species were weakly involved in the photocatalytic reaction. Consequently, h^+ plays a major role in dye degradation, as reported for the Fe_3O_4/BiOI catalyst.[40] Under UV irradiation, the catalysts mainly absorb incident UV light and directly create an electron and hole in the CB and VB of the $CoFe_2O_4$/BiOX catalysts, respectively. The electrons in the CBs of the catalysts commonly initiate the creation of active species. Therefore, the catalytic activities were not much different than those found under visible light, as shown in Fig. 11.

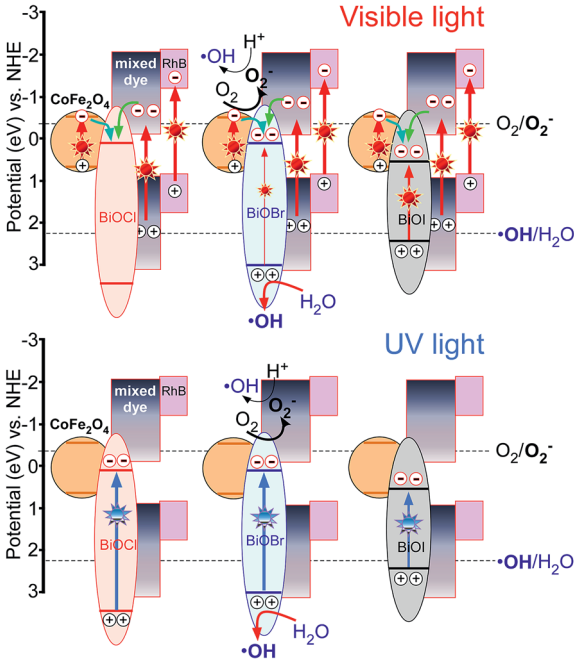

Fig. 14 Photocatalytic dye degradation mechanism of a dye over the $CoFe_2O_4$/BiOX (X = Cl, Br and I) microflowers. The red and blue vertical arrows indicate direct UV and visible light absorptions, respectively.

Finally, we tested reliability and stability of the catalyst samples after the photocatalytic dye degradation experiments.

We found that the crystal structure of the catalyst samples showed no change after photocatalytic dye degradation experiments. This indicates that the catalysts were very stable based on the XRD patterns (ESI, Fig. S7†). We tested the reusability of the catalysts samples, and found that about 80% of the initial performance was obtained in the second cycle. It took more time to completely photo-dissociate dye in a solution (ESI, Fig. S8†). This is due to some aggregation of the magnetic catalyst particles. However, in the third cycle the catalytic activity showed no significant decrease compared with the second cycle.

4. Conclusion

Highly efficient recyclable magnetic $CoFe_2O_4$/BiOX (X = Cl, Br and I) microflower photocatalysts were prepared by a solvothermal method and tested with a mixed dye (MO + RhB + MB) and pure MO, RhB and MB. The adsorption performance and photocatalytic activity of a photocatalyst for a complicated polluted system were examined. Several new important results are listed below.

(1) A saturation magnetization of 62.3 emu g^{-1} was measured for $CoFe_2O_4$ NPs. The magnetization values were decreased by 8–10× upon hybridization.

(2) For the adsorption of RhB, the adsorption performance showed an order of $CoFe_2O_4$/BiOBr < $CoFe_2O_4$/BiOCl ≪ $CoFe_2O_4$/BiOI. The adsorption capacity of $CoFe_2O_4$/BiOI was 160 mg g_{cat}^{-1}, which is much larger than <5 mg g_{cat}^{-1} for $CoFe_2O_4$/BiOCl and $CoFe_2O_4$/BiOBr.

(3) For the photocatalytic activity of pure RhB over $CoFe_2O_4$/BiOX microflowers, the photocatalytic activity showed an order of $CoFe_2O_4$/BiOBr < $CoFe_2O_4$/BiOCl < $CoFe_2O_4$/BiOI.

(4) The adsorption capacities of $CoFe_2O_4$/BiOI for MO and MB were 24 and 21 mg g_{cat}^{-1}, respectively. For pure MO and MB, the adsorption and photocatalytic degradation performances showed orders of $CoFe_2O_4$/BiOCl < $CoFe_2O_4$/BiOBr < $CoFe_2O_4$/BiOI and $CoFe_2O_4$/BiOBr < $CoFe_2O_4$/BiOCl < $CoFe_2O_4$/BiOI, respectively.

(5) The adsorptions in the mixed dye were different. In the mixed dye, MB showed the best adsorption over the $CoFe_2O_4$/BiOI microflowers while MO showed the best adsorption over the $CoFe_2O_4$/BiOCl and $CoFe_2O_4$/BiOBr microflowers. On the other hand, RhB was the most poorly adsorbed on the $CoFe_2O_4$/BiOX microflowers.

(6) The degradation rate of each dye in the mixed system was different. The MO dye was removed most easily by the catalysts under UV and visible light exposure. $CoFe_2O_4$/BiOBr showed the highest photocatalytic activity for MO degradation while $CoFe_2O_4$/BiOI showed the highest activity for RhB and MB degradation.

(7) For $CoFe_2O_4$/BiOX microflowers, h^+ and $^{\bullet}O_2^-$ play major and minor roles in photodegradation of the dyes, respectively. Although the $^{\bullet}OH$ radical was formed for $CoFe_2O_4$/BiOBr and $CoFe_2O_4$/BiOCl under visible light, the role was found to be negligible. No $^{\bullet}OH$ radical was formed for $CoFe_2O_4$/BiOI both under UV and visible light irradiations.

The newly developed magnetic photocatalysts provide new insights into the design of recyclable adsorbents and photocatalysts for a more complicated polluted system.

Acknowledgements

This study was supported financially by the National Research Foundation of Korea (NRF) grant funded by the Korean government (MEST) (NRF-2014R1A1A2055923).

References

1 L. Ye, Y. Su, X. Jin, H. Xie and C. Zhang, *Environ. Sci.: Nano*, 2014, **1**, 90–112.
2 H. Cheng, B. Huang and Y. Dai, *Nanoscale*, 2014, **6**, 2009–2026.
3 H. Zhao, F. Tian, R. Wang and R. Chen, *Reviews in Advanced Sciences and Engineering*, 2014, **3**, 3–27.
4 J. Li, Y. Yu and L. Zhang, *Nanoscale*, 2014, **6**, 8473–8488.
5 L. Zhang, W. Wang, S. Sun, Y. Sun, E. Gao and J. Xu, *Appl. Catal., B*, 2013, **132–133**, 315–320.
6 K. Li, Y. Tang, Y. Xu, Y. Wang, Y. Huo, H. Li and J. Jia, *Appl. Catal., B*, 2013, **140–141**, 179–188.
7 J. Xiong, G. Cheng, F. Qin, R. Wang, H. Sun and R. Chen, *Chem. Eng. J.*, 2013, **220**, 228–236.
8 J. Hu, S. Weng, Z. Zheng, Z. Pei, M. Huang and P. Liu, *J. Hazard. Mater.*, 2014, **264**, 293–302.
9 S. Wang, L. Wang, W. Ma, D. Johnson, Y. Fang, M. Jia and Y. Huang, *Chem. Eng. J.*, 2015, **259**, 410–416.
10 L. Ai, Y. Zeng and J. Jiang, *Chem. Eng. J.*, 2014, **235**, 331–339.
11 W. Kim, D. Pradhan, B. Min and Y. Sohn, *Appl. Catal., B*, 2014, **147**, 711–725.
12 Y. Park, Y. Na, D. Pradhan, B. Min and Y. Sohn, *CrystEngComm*, 2014, **16**, 3155–3167.
13 X. Zhang, X. Liu, C. Fan, Y. Wang, Y. Wang and Z. Liang, *Appl. Catal., B*, 2013, **132–133**, 332–341.
14 H. Cheng, B. Huang, X. Qin, X. Zhang and Y. Dai, *Chem. Commun.*, 2012, **48**, 97–99.
15 C. Zheng, C. Cao and Z. Ali, *Phys. Chem. Chem. Phys.*, 2015, **17**, 13347–13354.
16 L. Ye, J. Liu, Z. Jiang, T. Peng and L. Zan, *Appl. Catal., B*, 2013, **142–143**, 1–7.
17 C. Yu, F. Cao, G. Li, R. Wei, J. Yu, R. Jin, Q. Fan and C. Wang, *Sep. Sci. Technol.*, 2013, **120**, 110–122.
18 L. Lu, L. Kong, Z. Jiang, H. Lai, T. Xiao and P. Edwards, *Catal. Lett.*, 2012, **142**, 771–778.
19 T. Li, S. Luo and L. Yang, *J. Solid State Chem.*, 2013, **206**, 308–316.
20 Y. Lei, G. Wang, P. Guo and H. Song, *Appl. Surf. Sci.*, 2013, **279**, 374–379.
21 F. Li, Q. Wang, X. Wang, B. Li, Y. Hao, R. Liu and D. Zhao, *Appl. Catal., B*, 2014, **150–151**, 574–584.
22 H. Li, Y. Cui and W. Hong, *Appl. Surf. Sci.*, 2013, **264**, 581–588.
23 X. Zhang, T. Guo, X. Wang, Y. Wang, C. Fan and H. Zhang, *Appl. Catal., B*, 2014, **150–151**, 486–495.

24 J. Cao, B. Xu, H. Lin and S. Chen, *Chem. Eng. J.*, 2013, **228**, 482–488.
25 Z. Cui, M. Si, Z. Zheng, L. Mi, W. Fa and H. Jia, *Catal. Commun.*, 2013, **42**, 121–124.
26 C. Chang, L. Zhu, Y. Fu and X. Chu, *Chem. Eng. J.*, 2013, **233**, 305–314.
27 M. Su, C. He, L. Zhu, Z. Sun, C. Shan, Q. Zhang, D. Shu, R. Qiu and Y. Xiong, *J. Hazard. Mater.*, 2012, **229–230**, 72–82.
28 X. Wei, H. Cui, S. Guo, L. Zhao and W. Li, *J. Hazard. Mater.*, 2013, **263**, 650–658.
29 R. Wang, G. Jiang, X. Wang, R. Hu, X. Xi, S. Bao, Y. Zhou, T. Tong, S. Wang, T. Wang and W. Chen, *Powder Technol.*, 2012, **228**, 258–263.
30 X. Zhang, X. Chang, M. Gondal, B. Zhang, Y. Liu and G. Ji, *Appl. Surf. Sci.*, 2012, **258**, 7826–7832.
31 Z. Wu, W. Li, P. A. Webley and D. Zhao, *Adv. Mater.*, 2012, **24**, 485–491.
32 T. Xie, L. Xu, C. Liu, J. Yang and M. Wang, *Dalton Trans.*, 2014, **43**, 2211–2220.
33 Y. Yao, W. Huang, H. Zhou, Y. Zheng and X. Song, *J. Nanopart. Res.*, 2014, **16**, 2451–2459.
34 L. Zhang, W. Wang, S. Sun, Y. Sun, E. Gao and Z. Zhang, *Appl. Catal., B*, 2014, **148–149**, 164–169.
35 L. Zhang, W. Wang, L. Zhou, M. Shang and S. Sun, *Appl. Catal., B*, 2009, **90**, 458–462.
36 C. Tan, G. Zhu, M. Hojamberdiev, C. Xu, J. Liang, P. Luo and Y. Liu, *J. Cluster Sci.*, 2013, **24**, 1115–1126.
37 Y. Yao, W. Huang, H. Zhou, H. Yin, Y. Zheng and X. Song, *Mater. Chem. Phys.*, 2014, **148**, 896–902.
38 C. Guo, Y. He, P. Du, X. Zhao, J. Lv, W. Meng, Y. Zhang and J. Xu, *Appl. Surf. Sci.*, 2014, **320**, 383–390.
39 L. Kong, Z. Jiang, T. Xiao, L. Lu, M. Jones and P. Edwards, *Chem. Commun.*, 2011, **47**, 5512–5514.
40 X. Li, C. Niu, D. Huang, X. Wang, X. Zhang, G. Zeng and Q. Niu, *Appl. Surf. Sci.*, 2013, **286**, 40–46.
41 J. Xu, W. Meng, Y. Zhang, L. Li and C. Guo, *Appl. Catal., B*, 2011, **107**, 355–362.
42 J. Xu, L. Li, C. Guo, Y. Zhang and W. Meng, *Appl. Catal., B*, 2013, **130–131**, 285–292.
43 X. Wang, W. Yang, F. Li, J. Zhao, R. Liu, S. Liu and B. Li, *J. Hazard. Mater.*, 2015, **292**, 126–136.
44 M. Kooti and E. Nasiri, *J. Mol. Catal. A: Chem.*, 2015, **406**, 168–177.
45 Z. Cai, Y. J. Liu, X. Lu and J. Teng, *J. Phys. Chem. C*, 2013, **117**, 9440–9445.
46 Z. Cai, J. Teng, Z. Xiong, Y. Li, Q. Li, X. Lu and X. S. Zhao, *Langmuir*, 2011, **27**, 5157–5164.
47 B. Tian, T. Wang, R. Dong, S. Bao, F. Yang and J. Zhang, *Appl. Catal., B*, 2014, **147**, 22–28.
48 Z. Cai, Z. Xiong, X. Lu and J. Teng, *J. Mater. Chem. A*, 2014, **2**, 545–553.
49 J. Cao, B. Xu, H. Lin, B. Luo and S. Chen, *Chem. Eng. J.*, 2012, **185–186**, 91–99.
50 M. Yin, Z. Li, J. Kou and Z. Zou, *Environ. Sci. Technol.*, 2009, **43**, 8361–8366.
51 X. Qin, H. Cheng, W. Wang, B. Huang, X. Zhang and Y. Dai, *Mater. Lett.*, 2013, **100**, 285–288.
52 J. Jiang, K. Zhao, X. Xiao and L. Zhang, *J. Am. Chem. Soc.*, 2012, **134**, 4473–4476.
53 D. Zhang, J. Li, Q. Wang and Q. Wu, *J. Mater. Chem. A*, 2013, **1**, 8622–8629.
54 Y. Li, J. Wang, H. Yao, L. Dang and Z. Li, *J. Mol. Catal. A: Chem.*, 2011, **334**, 116–122.
55 K. Vignesha, A. Suganthi, B. Min and M. Kang, *Appl. Surf. Sci.*, 2015, **324**, 652–661.
56 C. Yu, F. Cao, G. Li, R. Wei, J. Yu, R. Jin, Q. Fan and C. Wang, *Sep. Purif. Technol.*, 2013, **120**, 110–122.
57 Y. I. Choi, H. J. Jung, W. G. Shin and Y. Sohn, *Appl. Surf. Sci.*, 2015, **356**, 615–625.
58 M. J. Kim, Y. I. Choi, S. W. Joo, M. Kang and Y. Sohn, *Ceram. Int.*, 2014, **40**, 16051–16059.
59 Y. Na, Y. I. Kim, D. W. Cho, D. Pradhan and Y. Sohn, *Mater. Sci. Semicond. Process.*, 2014, **27**, 181–190.
60 N. Roy, Y. Park, Y. Sohn, K. T. Leung and D. Pradhan, *ACS Appl. Mater. Interfaces*, 2014, **6**, 16498–16507.
61 Y. Na, S. W. Lee, N. Roy, D. Pradhan and Y. Sohn, *CrystEngComm*, 2014, **16**, 8546–8554.
62 A. K. Nayak, S. Lee, Y. Sohn and D. Pradhan, *CrystEngComm*, 2014, **16**, 8064–8072.
63 M. M. Khan, S. A. Ansari, M. O. Ansari, B. K. Min, J. Lee and M. H. Cho, *J. Phys. Chem. C*, 2014, **118**, 9477–9484.
64 B. Holinsworth, D. Mazumdar, H. Sims, Q. Sun, M. Yurtisigi, S. Sarker, A. Gupta, W. Butler and J. Musfeldt, *Appl. Phys. Lett.*, 2013, **103**, 082406–082409.
65 L. Ye, L. Tian, T. Peng and L. Zan, *J. Mater. Chem.*, 2011, **21**, 12479–12484.